

Nondegenerate parametric oscillations in a tunable superconducting resonator

Andreas Bengtsson,^{1,*} Philip Krantz,² Michaël Simoen,¹ Ida-Maria Svensson,¹
Ben Schneider,¹ Vitaly Shumeiko,¹ Per Delsing,¹ and Jonas Bylander^{1,†}

¹*Microtechnology and Nanoscience, Chalmers University of Technology, SE-412 96, Göteborg, Sweden*

²*Research Laboratory of Electronics, Massachusetts Institute of Technology, Cambridge, MA 02139, USA*

(Dated: January 16, 2018)

We investigate nondegenerate parametric oscillations in a multimode superconducting microwave resonator that is terminated by a SQUID. The parametric effect is achieved by modulating magnetic flux through the SQUID at a frequency close to the sum of two resonator-mode frequencies. For modulation amplitudes exceeding an instability threshold, self-sustained oscillations are observed in both modes. The amplitudes of these oscillations show good quantitative agreement with a theoretical model. The oscillation phases are found to be correlated and exhibit strong fluctuations which broaden the oscillation spectral linewidths. These linewidths are significantly reduced by applying a weak on-resonance tone, which also suppresses the phase fluctuations. When the weak tone is detuned, we observe synchronization of the oscillation frequency with the frequency of the input. For the detuned input, we also observe an emergence of three idlers in the output. This observation is in agreement with theory indicating four-mode amplification and squeezing of a coherent input.

I. INTRODUCTION

The circuit quantum electrodynamics architecture (cQED)¹ is an attractive platform for quantum information processing with continuous variables. Within cQED, a variety of nonclassical photonic states can be efficiently generated by nonlinear superconducting elements — superpositions of Fock states,² entangled two-mode photonic states,^{3–5} and multi-photon cat states.⁶ Parametric phenomena have played important roles in this development.

A typical cQED parametric device consists of a high-quality superconducting resonator integrated with Josephson elements that induce a Kerr nonlinearity in the resonator, and also allow for rapid modulation of the resonator frequency.^{7–10}

By means of such a modulation, at a frequency twice the resonator mode frequency, a degenerate Josephson parametric oscillator (JPO) regime is achieved.¹¹ The JPO can be used for vacuum squeezing and photonic entanglement,^{12,13} photonic qubit operation,¹⁴ and cat state engineering.^{15–17} The JPO has also been employed for high-fidelity readout of superconducting qubits.^{18,19}

In this paper, we report on an experimental investigation of a different regime, the nondegenerate Josephson parametric oscillator (NJPO). In this regime, self-sustained oscillations of two resonator modes, n and m , are excited by modulating the Josephson inductance at a frequency close to the sum of the mode frequencies, $\omega_p \approx \omega_n + \omega_m$. A detailed theory of nondegenerate parametric resonance has been developed in Ref. 20. The NJPO establishes at parametric pump amplitudes above a critical value, where instability of the resonator ground state develops and is stabilized by the Kerr nonlinearity. Some properties of the nondegenerate parametric resonance in the sub-threshold region — amplification^{5,21} and frequency-conversion^{22,23} have been experimentally investigated.

Our interest to the NJPO is driven by potentially novel, compared to the JPO, quantum statistical properties of the generated field. The novelty is related to a presence of additional idlers and multimode squeezing,²⁰ and large phase fluctuations resulting from a continuous degeneracy of the oscillator state. The latter is analogous to an extensively studied effect in optical paramet-

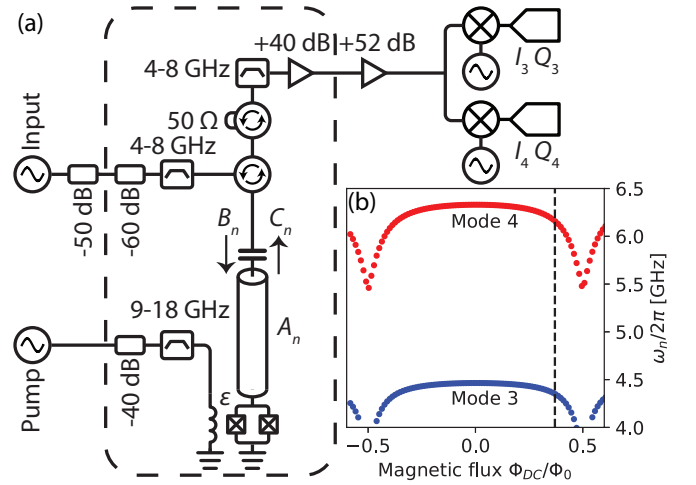


FIG. 1. (a) Schematic of the experimental setup, where the dashed box indicates the dilution refrigerator. The device consists of a capacitively coupled resonator shorted to ground via a SQUID. The magnetic flux through the SQUID is modulated with an effective amplitude ϵ , via an on-chip microwave line. There are three types of fields present in the system: in-resonator fields A_n , input fields B_n , and outgoing fields C_n , where the last two are separated by a microwave circulator. The outgoing fields are amplified and split to two vector digitizers measuring the quadratures I_n and Q_n . (b) Measured resonant frequencies for modes 3 (blue) and 4 (red) as a function of magnetic flux through the SQUID loop. The vertical dashed line marks the static flux bias, $\Phi_{DC} = 0.37\Phi_0$, used to generate nondegenerate parametric oscillations.

ric oscillators.^{24–32} To date, neither classical nor quantum properties of the NJPO have been experimentally verified. The aim of this work is to fill this gap. We investigate quasiclassical dynamics of the NJPO: intensity and frequency of the oscillations as functions of the pump parameters, properties of the phase dynamics, and response to external coherent inputs.

II. EXPERIMENTAL METHODS

The device investigated is a coplanar waveguide resonator, capacitively coupled to a transmission line at one end, and shorted to ground via a dc superconducting quantum interference device (SQUID) at the other end, see Fig. 1(a). The resonator is reactive-ion etched from a sputtered thin-film of niobium on a high-resistivity silicon substrate. The SQUID is deposited with a two-angle evaporation of aluminum. The layout of the device is similar to that in Ref. 21. The distance between the interdigitated coupling capacitor and the SQUID is 31 mm, yielding a fundamental resonant frequency $\omega_1/2\pi = 912$ MHz. The available measurement frequency window is 4–8 GHz, limited by the microwave setup, giving experimental access to the higher resonator modes with numbers 3, 4, and 5. A setup schematic is shown in Fig. 1(a). The device is mounted at the mixing chamber of a dilution refrigerator with a base temperature of 10 mK.

The magnetic field through the SQUID loop can be applied statically via an external coil, or modulated via an on-chip flux line. The resonant frequencies for modes 3 and 4, as functions of the static magnetic flux Φ_{DC} , are shown in Fig. 1(b).

Each mode of the NJPO is characterized by the resonant frequency ω_n , external loss rate Γ_{n0} , total loss rate Γ_n , and Kerr coefficient α_n . The resonant frequencies and loss rates are determined by data fitting of measured complex reflection coefficients. At the static flux bias $\Phi_{\text{DC}} = 0.37\Phi_0$ indicated in Fig. 1(b), we find $\omega_3/2\pi = 4.345$ GHz, $\omega_4/2\pi = 6.150$ GHz, $\Gamma_{30}/2\pi = 0.52$ MHz, $\Gamma_3/2\pi = 0.56$ MHz, $\Gamma_{40}/2\pi = 0.70$ MHz, and $\Gamma_4/2\pi = 0.78$ MHz. The Kerr coefficients are determined from properties of the parametric oscillations and explained later.

A microwave signal generator supplies the coherent pump tone to the on-chip flux line via an attenuated and filtered coaxial line. The output of the resonator is routed through microwave filters and two circulators to a cryogenic low-noise amplifier. The output is further amplified at room temperature before detection. Additionally, to investigate the system response, an input field can be applied to resonator via the first circulator.

The quadrature voltages of the output are acquired by heterodyne detection. The use of two sets of digitizers, mixers, and local oscillators, allows for a simultaneous detection of two modes far separated in frequency. From each digitizer, we transfer the digitally downconverted quadrature voltages to a computer for further

processing. The output power from each mode, P_n , is calculated and related to the output photon flux $|C_n|^2$, $|C_n|^2 = (P_n - P_{\text{noise}})/(G\hbar\omega_d)$, where P_{noise} is the system noise power measured with the pump off, and ω_d is the detection frequency. The system gain G , is calibrated at each mode frequency using a shot-noise tunnel junction.³³ In a similar way, the quadrature voltages are converted to dimensionless quantities, $I_n(t)$ and $Q_n(t)$, corresponding to the square root of the number of photons per second and unit bandwidth.

III. RESULTS

A. Parametric oscillations

We excite the parametric resonance by modulating the SQUID inductance at a frequency close to the sum of the frequencies of modes 3 and 4, $\omega_p = \omega_3 + \omega_4 + 2\delta$, where δ refers to the pump detuning. The quantum resonant two-mode dynamics is generally described with a Hamiltonian written in a doubly rotating frame with frequencies $\omega_{3,4} + \delta$,^{12,20}

$$H/\hbar = - \sum_{n=3,4} [\delta a_n^\dagger a_n + (\alpha_n/2)(a_n^\dagger a_n)^2] - 2\alpha(a_3^\dagger a_3 a_4^\dagger a_4) - \epsilon(a_3 a_4 + a_3^\dagger a_4^\dagger), \quad (1)$$

where a_n is the annihilation operator of the in-resonator field of mode n , ϵ is the effective amplitude of the parametric pump, and $\alpha = \sqrt{\alpha_3 \alpha_4}$ is the cross-Kerr coefficient.

Throughout this work, we restrict our interpretation of experimental data to a quasiclassical model of the resonator dynamics, which operates with the classical field amplitudes $A_n(t)$. The amplitudes satisfy two dynamical equations,

$$i\dot{A}_3 + (\zeta_3 + i\Gamma_3)A_3 + \epsilon A_4^* = \sqrt{2\Gamma_{30}}B_3(t), \\ i\dot{A}_4 + (\zeta_4 + i\Gamma_4)A_4 + \epsilon A_3^* = \sqrt{2\Gamma_{40}}B_4(t), \quad (2)$$

where $B_n(t)$ is an external driving field, and ζ_n is a nonlinear detuning including the Kerr-induced frequency shifts,

$$\zeta_3 = \delta + \alpha_3|A_3|^2 + 2\alpha|A_4|^2, \\ \zeta_4 = \delta + \alpha_4|A_4|^2 + 2\alpha|A_3|^2. \quad (3)$$

The normalization of the field amplitudes, $|A_n|^2$ and $|B_n|^2$, corresponds to the number of photons in respective mode and the incoming photon flux, respectively. Parametric self-sustained oscillations correspond to non-trivial solutions of the homogeneous nonlinear equations (2) and (3).

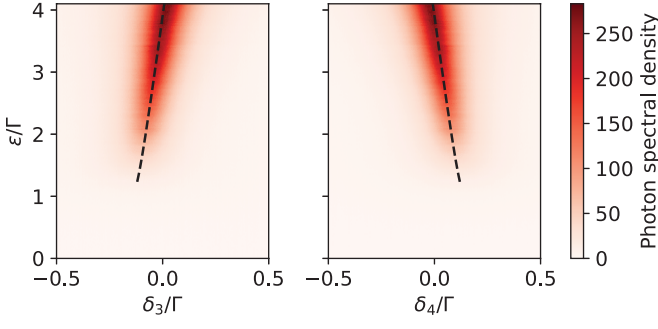


FIG. 2. Parametric instability. Measured photon spectral densities of the output from mode 3 (left) and 4 (right). The parametric pump has an amplitude ϵ , and is applied at a detuning $\delta = 0.26\Gamma$. The detection frequency detunings δ_n , is relative to the respective rotating frame. The dashed lines are the radiation frequencies from Eq. (5).

1. Parametric instability

By ramping the pump amplitude we observe a strong increase of the output photon flux above a certain pump threshold, as shown in Fig. 2. The radiation is detected at frequencies ω_d , associated with the excited resonator modes but deviating from the respective rotating frames, $\delta_n = \omega_d - (\omega_n + \delta)$, in good agreement with a theoretical prediction,²⁰

$$\delta_3 = -\delta_4 = \delta \frac{\Gamma_3 - \Gamma_4}{\Gamma_3 + \Gamma_4}. \quad (4)$$

With further increase of the pump power, the radiation frequencies shift, as shown in Fig. 2. This shift is accurately described by the equation,²⁰

$$\delta_3(\epsilon) = -\delta_4(\epsilon) = \Delta_0 = \frac{\Gamma_3\zeta_4 - \Gamma_4\zeta_3}{\Gamma_3 + \Gamma_4}. \quad (5)$$

The instability of the resonator ground state occurs within an interval of the pump detuning,

$$|\delta| < \delta_{\text{th}}(\epsilon) = \frac{\Gamma_3 + \Gamma_4}{2} \sqrt{\frac{\epsilon^2}{\Gamma^2} - 1}. \quad (6)$$

This criterion defines three regions in the ϵ - δ plane, as presented in Fig. 3:

- (I) at $\epsilon < \Gamma$ or $\delta > \delta_{\text{th}}(\epsilon)$ only the ground state, $A_n = 0$, is stable;
- (II) at $\epsilon > \Gamma$ and $|\delta| < \delta_{\text{th}}(\epsilon)$ the ground state is unstable and self-sustained oscillations emerge;
- (III) at $\epsilon > \Gamma$ and $\delta < -\delta_{\text{th}}(\epsilon)$ the ground state regains stability while the self-sustained oscillations persist — this is a bistability region.

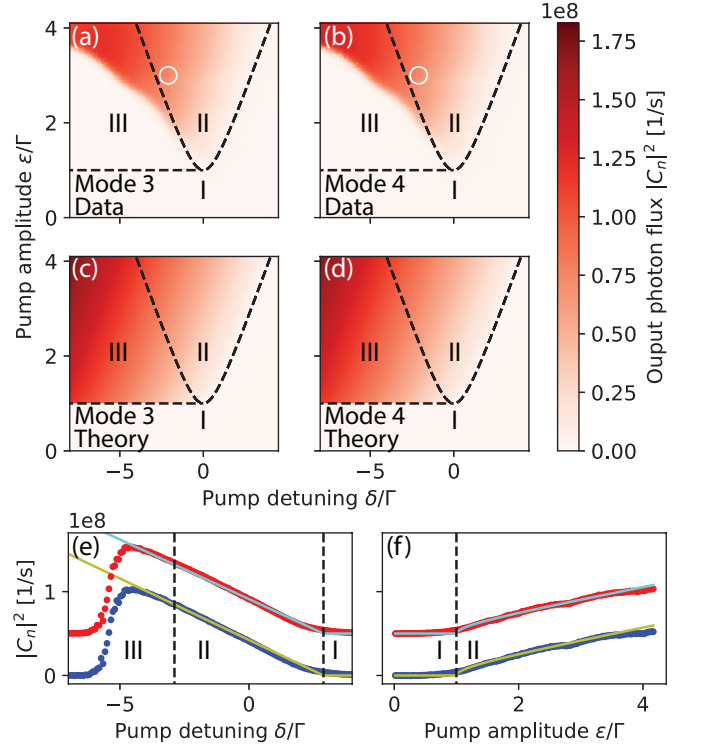


FIG. 3. Nondegenerate pumping of modes $n = 3$ and 4 , at the frequency $\omega_p = \omega_3 + \omega_4 + 2\delta$. Experimentally measured (a-b), and theoretically calculated (c-d), output intensities $|C_n|^2$ vs. pump detuning δ and amplitude ϵ . I-III indicate the three different stability regions described in the main text. (e) Horizontal line cuts of (a-d) at $\epsilon = 3\Gamma$, where mode 4 is offset in the positive y-direction for clarity. The dots are measured values and solid lines are from theory. (f) Vertical line cuts of (a-d) at $\delta = 0$, where mode 4 is offset in the positive y-direction for clarity. The dots are measured values and solid lines are from theory.

2. Output intensities

A quantitative analysis of the intensity of the oscillations is performed by solving Eq. (2),

$$|A_3|^2 = \frac{2\Gamma_4(\delta_{\text{th}}(\epsilon) - \delta)}{\alpha_3\Gamma_4 + \alpha_4\Gamma_3 + 2\alpha(\Gamma_3 + \Gamma_4)}, \quad (7)$$

$$|A_4|^2 = \frac{\Gamma_3}{\Gamma_4} |A_3|^2. \quad (8)$$

The output intensity is given by the relation $|C_n|^2 = 2\Gamma_{n0}|A_n|^2$; for the experimentally extracted external and total losses, $|C_3|^2 \approx |C_4|^2$.

In Fig. 3, the measured output intensities are shown on panels (a) and (b), while panels (c) and (d) show the computed intensities of the oscillations. In the bistability region III, the output intensities decrease with red detuning, indicating a system preference to occupy the ground state. Measured output intensities, as a function of the pump detuning at a fixed pump amplitude $\epsilon = 3\Gamma$, are presented in Fig. 3(e). The data and the theory are in

excellent agreement in region II and down to $\delta \approx -4.5\Gamma$ in region III, implying that the system is mostly in the excited state. Below $\delta \approx -4.5\Gamma$, the occupancy of the excited state rapidly decreases. Figure 3(f) illustrates the growth of the output intensities with the pump amplitude at $\delta = 0$, also showing good agreement with the theory.

The slopes of the frequency shift in Fig. 2 and the output intensity in Fig. 3(e), together with Eqs. (5) and (7), are used to extract the Kerr coefficients as well as the conversion coefficient between the flux pump amplitude and ϵ . The extracted values for the Kerr coefficients are $\alpha_3/2\pi = 71$ kHz and $\alpha_4/2\pi = 178$ kHz.

3. Phase dynamics

We further investigate the phase properties of the parametric oscillations. To this end, we choose the point in the δ - ϵ space indicated by the white circles in Fig. 3(a-b), and acquire 1 million samples for the quadratures $I_n(t)$ and $Q_n(t)$, during 2.5 seconds of measurement time. By creating two-dimensional histograms, we present the data in Fig. 4(a-b). The oscillations have a finite average amplitude, while the phase is evenly distributed between $-\pi$ and π . This observation supports the theoretical prediction about a continuous degeneracy of the oscillator state with respect to the phase.²⁰ More precisely, the oscillator phases $|A_n|e^{i\theta_n}$, respect the constraint,

$$\begin{aligned} \theta_3 + \theta_4 &= \Theta, \quad \Theta \in \{\pi/2, \pi\}, \\ \tan \Theta &= -\frac{1}{\sqrt{\epsilon^2/\Gamma^2 - 1}}, \end{aligned} \quad (9)$$

while the difference of the phases, $\psi = \theta_3 - \theta_4$, is arbitrary. Such a degeneracy gives rise to phase diffusion under the effect of vacuum fluctuations, which underlines the broadening of the spectrum of the output signal in Fig. 2.

To reveal the intermode phase correlation, we synchronize the digitizers by using a common trigger. This allows us to create the cross-quadrature histograms, I_3, I_4 and Q_3, Q_4 , in an analogous way to the phase-space distributions. Fig. 4(c-d) present the cross-quadrature histograms for quadratures chosen such that their common output phase Θ is compensated by the phases of the local oscillators. With such a choice, the histograms exhibit the relations, $I_3 = I_4$, and $Q_3 = -Q_4$. To further illustrate the phase anti-correlation property, we plot in Fig. 4(e), a time evolution realization of the phases of the two modes.

The effective frequency-noise spectrum can be extracted from the phase evolution. It is presented for mode 3 in Fig. 4(f). The spectrum is in good agreement with a $1/f$ component combined with white noise. The origin of the low-frequency noise is most likely due to flux noise through the SQUID loop, which is known to have a $1/f$ spectrum.³⁴

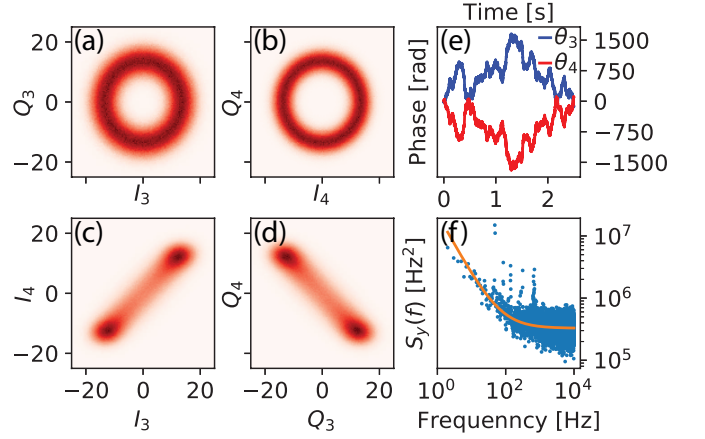


FIG. 4. Phase-space distributions for nondegenerate parametric oscillations measured at the point indicated by the white circles in Fig. 2. Panels (a-b) show the distributions for modes 3 and 4. The color scale is proportional to the number of counts in each bin. (c-d) Two out of four cross-quadrature histograms, showing clear anti-correlation between the mode phases θ_n . (e) Evolution of the phases θ_n in time. (f) Frequency-noise spectrum of the parametric oscillations in mode 3. The solid line shows a combination of $1/f$ and white noise.

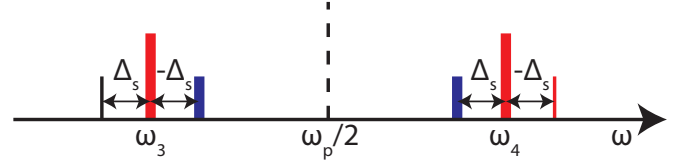


FIG. 5. Frequency diagram of the four-mode amplification. The dashed line is the parametric pump, the bold red lines are the parametric oscillations, the thin black line is the coherent signal, the thin red line is the primary idler, and the bold blue lines are the secondary idlers.

B. Response to an external signal

In this section, we explore the response of the NJPO to an external coherent input. Linear response of parametric systems to weak external signals underlines many properties of quantum noise. For instance, the presence of an idler in parametric amplification below the threshold, defines the structure of squeezed vacuum and two-mode entanglement of output photons.³⁻⁵ This is true for both degenerate and nondegenerate parametric resonance, with the only difference that for the nondegenerate case, the idler has a frequency far detuned from the signal frequency and appears within the bandwidth of the conjugated mode,²¹ while for the degenerate case, the idler appears within the bandwidth of the signal mode.

Above the threshold, the situation is qualitatively similar for the JPO.¹² However, for the NJPO, the situation is quite different. Here, the strong fields produced by the parametric oscillations in the two resonator modes generate, through a four-mode mixing mechanism, two

additional idlers,²⁰ see Fig. 5. The intensity of these secondary idlers are proportional to the oscillation intensities $|A_n|^2$, while the intensity of the primary idler is defined by, and proportional to, the flux pump intensity ϵ^2 . This process of four-mode amplification should result in a four-mode quantum noise squeezing. The output noise should also be influenced by the strong fluctuations of the oscillation phases discussed above.

In this section, we present data that corroborate the presence of the three idlers in the NJPO response. In addition, we observe two effects that imply a strong influence of the input signal on the oscillator phase dynamics — phase locking, and frequency synchronization.

1. Injection locking

It is generally known that in self-sustained oscillators possessing phase degeneracy, large phase fluctuations can be suppressed by injecting a small, but frequency stable, signal on-resonance with the oscillator.³⁵ This effect is explained by a violation of the symmetry underlining the phase degeneracy by external driving. The phase locking effect has been observed in a nondegenerate optical parametric oscillator.³⁶ For our system, it has been shown,²⁰ that applying an input with the same frequency as the oscillator frequency, locks the oscillator phase to the value defined by the phase of the input, θ_{in} ,

$$\theta_3 = \theta_{\text{in}} - \arctan \frac{3\Gamma}{2\sqrt{\epsilon^2 - \Gamma^2}}. \quad (10)$$

Due to the intermode phase coupling, Eq. (9), both modes are phase locked simultaneously.

We investigate this locking effect by injecting a coherent signal B_3 on resonance with the parametric oscillations in mode 3. We characterize the input field with an average number of coherent photons $\langle n \rangle = |B_3|^2 / (2\Gamma_{30})$. To quantify the efficiency of the injection locking, we measure the output spectral densities as functions of the input photon number $\langle n \rangle$, which is presented in Fig. 6(a-b). In Fig. 6(c), we plot line cuts for mode 3 for several injection photon numbers. For low input photon numbers, the radiation line is still broad, but when the input power is increased, the width is substantially reduced, and if increased further, the frequency noise is removed almost entirely. The -3 dB point is below the resolution bandwidth of 1 Hz, implying a frequency noise reduction of at least a factor 5000. This narrowing effect becomes pronounced at $\langle n \rangle \geq 0.5$, similarly to what was found to phase lock the JPO.¹⁸ This result can be understood from the following argument: under the effect of vacuum noise, the oscillator phase undergoes random motion, which is shown in Fig. 4(f) as the white frequency noise above 100 Hz. This random motion can only be constrained by a coherent input whose strength exceeds the intensity of the vacuum fluctuations, $\langle n \rangle = 1/2$.

Figure 7(a-f) illustrates the phase-space distributions for both modes at the same input powers as in Fig. 6(c).

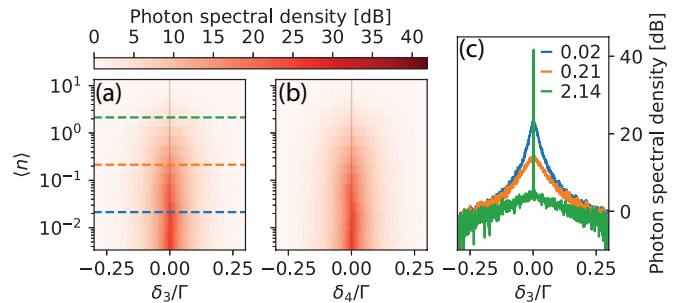


FIG. 6. Photon spectral densities of a nondegenerate parametric oscillator under injection locking. The scale is presented in a logarithmic unit relative to 1 photon/(sHz). Panels (a) and (b) show the output radiation for modes 3 and 4, respectively. δ_n is the detuning between the detection frequency and the center frequency of the radiation in the respective mode, and $\langle n \rangle$ is the average input photon number to mode 3. (c) Line cuts of (a) at the three input photon numbers indicated by the corresponding colored dashed lines in (a).

The calculated phase distributions and standard deviations are presented in Fig. 7(g) and (h), respectively, as functions of the input photon number. The phase distribution is uniform between $-\pi$ and π for small injection signals, and has a standard deviation close to that expected for a uniform distribution, $\pi/\sqrt{3}$. For increasing $\langle n \rangle$, the distribution approaches a Gaussian form, and the standard deviation saturates. It is difficult to compare the eventually locked phase with the theoretical value, Eq. (10), because of the difficulty of experimentally calibrating the phase accumulation between the resonator and the detectors.

2. Synchronization and secondary idlers

Applying an input signal detuned from the oscillation frequency, gives rise to the interesting and related phenomenon of frequency synchronization.^{35,37} We introduce a detuning Δ_s between the injection signal and the parametric oscillations in mode 3, and study the output photon spectral densities of both modes as functions of Δ_s and $\langle n \rangle$, see Fig. 8(a-d). Within a certain interval of detuning, we observe a sudden change of the oscillation frequency, which synchronizes with the frequency of the input. Simultaneously, the frequency of the conjugated mode synchronizes with the frequency of the primary idler. Due to the dramatic decrease of the linewidth of the synchronized output signal, the effect appears in Fig. 8(a-d) as a gap in frequency space where the oscillations have the same frequency as the locking signal. The gap size is proportional to the size of the synchronization detuning window, which in turn is proportional to the square root of the input power.³⁵ In Fig. 8(e), we quantify the gap size and find good agreement with the predicted square-root dependence.

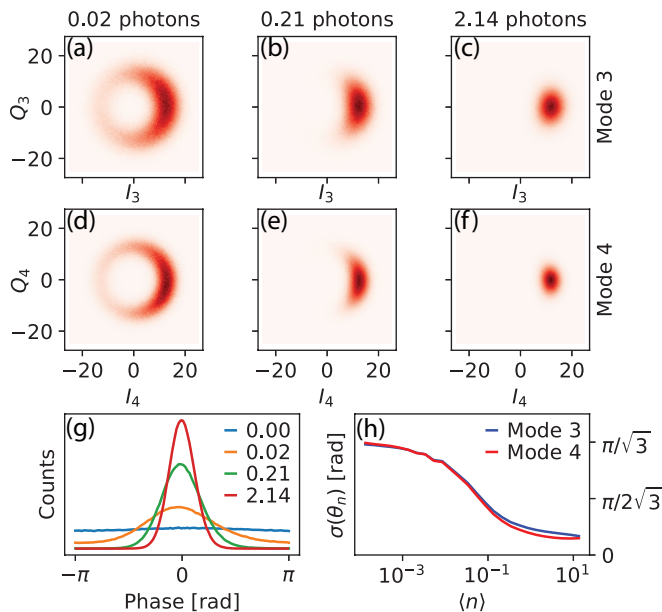


FIG. 7. Phase locking of nondegenerate parametric oscillations by signal injection. Phase-space histograms for the parametric radiation in modes 3 (a-c) and 4 (d-f), with a coherent signal injected into mode 3. The input photon number $\langle n \rangle$ is stated above each panel column, and are the same as in Fig. 6(c). The color scale is proportional to the number of counts in each bin. (g) Distributions of the phase of the parametric oscillations in mode 3, θ_3 , for different input photon numbers. (h) Standard deviation of the phases θ_n , as functions of the input photon number to mode 3.

Figure 8(a-d) also reveals the presence of three idlers in the output. The output signal in mode 3, seen as a thin diagonal line on panels (a) and (c) (hardly visible at the small intensity on panel (a)) generates a primary idler in mode 4, seen as a thin diagonal line in the opposite direction compared to the signal, on panels (b) and (d). This idler has its frequency detuned by $-\Delta_s$ from the oscillation frequency in this mode, and it has a small linewidth, similar to the signal. The two secondary idlers are visible on panels (a) to (d). The secondary idler on panels (a) and (c) is detuned by $-\Delta_s$ from the oscillation frequency of mode 3, while the secondary idler on panels (b) and (d) is detuned by Δ_s from the oscillation frequency of mode 4. These secondary idlers are generated by the in-resonator fields of the parametric oscillator, and they are much broader than the signal and primary idler, their linewidths are instead comparable to the one of the oscillations.

IV. CONCLUSION

In conclusion, we investigated a nondegenerate Josephson parametric oscillator, NJPO, using a tunable superconducting resonator. By modulating magnetic flux through the SQUID attached to the resonator, we gener-

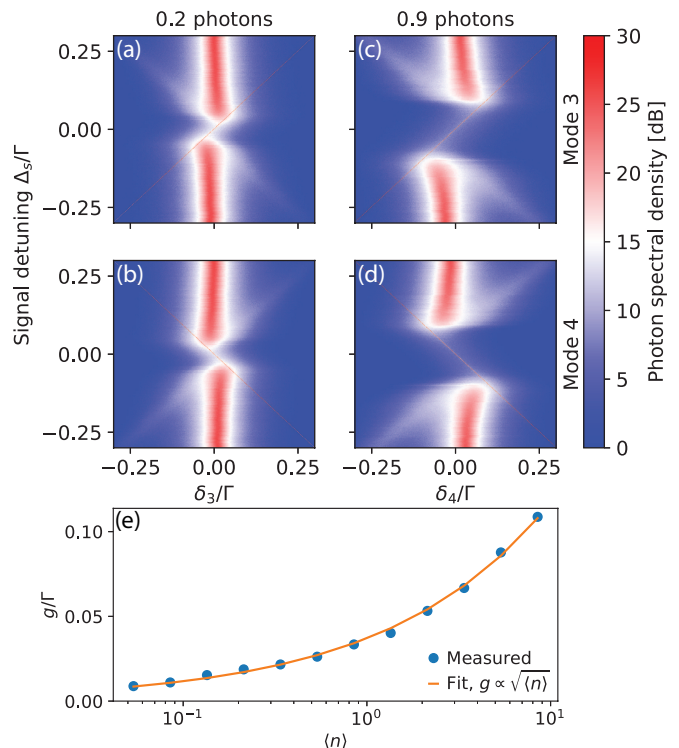


FIG. 8. Response of the parametric oscillations to a detuned signal. Panels (a-d) show the output photon spectral densities on a logarithmic scale, for mode 3 (a,c) and mode 4 (b,d). The detection detunings δ_n are relative to from the center of the parametric oscillations in the respective mode. The signal detuning Δ_s , is the detuning between the coherent signal and the center of the oscillation frequency in mode 3. The input photon number is stated above the two panel columns. Panel (e) shows the obtained size of the frequency gap g , and a fit to $g \propto \sqrt{\langle n \rangle}$.

ated intense correlated output radiation of two resonator modes. The measured radiation frequencies and intensities, as functions of the pump parameters, show excellent quantitative agreement with theory. A correlated phase dynamics of the oscillations was directly observed, and a continuous phase degeneracy of the oscillations was demonstrated. We also demonstrated significant suppression of the phase fluctuations when a weak on-resonance coherent signal was applied. Simultaneously, the oscillation linewidths were reduced by at least three orders of magnitude. In addition, the frequency synchronization effect was observed when the input signal was detuned from the resonance. Such an input was found to generate three output idlers in agreement with theoretical predictions.

Our findings form a solid ground for further exploration of the quantum properties of the NJPO field, that would exhibit four-mode squeezing and might possess non-Gaussian properties.

ACKNOWLEDGMENTS

We wish to express our gratitude to Waltraut Wustmann, Giulia Ferrini, Göran Johansson, and Jonathan Burnett for helpful discussions. We also thank José Au-

mentado for providing the shot-noise tunnel junction. We acknowledge financial support from the Knut and Alice Wallenberg foundation, and from the Swedish Research Council. J.B. acknowledges partial support by the EU under REA grant agreement no. CIG-618353.

-
- * andreas.bengtsson@chalmers.se
† jonas.bylander@chalmers.se
- ¹ R. J. Schoelkopf and S. M. Girvin, *Nature* **451**, 664 (2008).
 - ² M. Hofheinz, H. Wang, M. Ansmann, R. C. Bialczak, E. Lucero, M. Neeley, A. D. O’Connell, D. Sank, J. Wenner, J. M. Martinis, and A. N. Cleland, *Nature* **459**, 546 (2009).
 - ³ C. Eichler, D. Bozyigit, C. Lang, M. Baur, L. Steffen, J. M. Fink, S. Filipp, and A. Wallraff, *Phys. Rev. Lett.* **107**, 113601 (2011).
 - ⁴ E. Flurin, N. Roch, F. Mallet, M. H. Devoret, and B. Huard, *Phys. Rev. Lett.* **109**, 183901 (2012).
 - ⁵ C. W. Chang, M. Simoen, J. Aumentado, C. Sabín, P. Forn-Díaz, A. M. Vadiraj, F. Quijandria, G. Johansson, I. Fuentes, and C. M. Wilson, *arXiv preprint arXiv:1709.00083* (2017).
 - ⁶ B. Vlastakis, G. Kirchmair, Z. Leghtas, S. E. Nigg, L. Frunzio, S. M. Girvin, M. Mirrahimi, M. H. Devoret, and R. J. Schoelkopf, *Science* **342**, 607 (2013).
 - ⁷ M. Sandberg, C. M. Wilson, F. Persson, T. Bauch, G. Johansson, V. Shumeiko, T. Duty, and P. Delsing, *Appl. Phys. Lett.* **92**, 203501 (2008).
 - ⁸ T. Yamamoto, K. Inomata, M. Watanabe, K. Matsuba, T. Miyazaki, W. D. Oliver, Y. Nakamura, and J. Tsai, *Appl. Phys. Lett.* **93**, 042510 (2008).
 - ⁹ M. Wallquist, V. S. Shumeiko, and G. Wendin, *Phys. Rev. B* **74**, 224506 (2006).
 - ¹⁰ N. Bergeal, F. Schackert, M. Metcalfe, R. Vijay, V. E. Manucharyan, L. Frunzio, D. E. Prober, R. J. Schoelkopf, S. M. Girvin, and M. H. Devoret, *Nature* **465**, 64 (2010).
 - ¹¹ C. M. Wilson, T. Duty, M. Sandberg, F. Persson, V. Shumeiko, and P. Delsing, *Phys. Rev. Lett.* **105**, 233907 (2010).
 - ¹² W. Wustmann and V. Shumeiko, *Phys. Rev. B* **87**, 184501 (2013).
 - ¹³ C. H. Meaney, H. Nha, T. Duty, and G. J. Milburn, *EPJ Quantum Technology* **1**, 7 (2014).
 - ¹⁴ T. Inagaki, K. Inaba, R. Hamerly, K. Inoue, Y. Yamamoto, and H. Takesue, *Nat. Photonics* **10**, 415 (2016).
 - ¹⁵ S. Puri, S. Boutin, and A. Blais, *npj Quantum Inf.* **3**, 18 (2017).
 - ¹⁶ N. Bartolo, F. Minganti, W. Casteels, and C. Ciuti, *Phys. Rev. A* **94**, 033841 (2016).
 - ¹⁷ M. Mirrahimi, Z. Leghtas, V. V. Albert, S. Touzard, R. J. Schoelkopf, L. Jiang, and M. H. Devoret, *New J. Phys.* **16**, 045014 (2014).
 - ¹⁸ Z. R. Lin, K. Inomata, K. Koshino, W. D. Oliver, Y. Nakamura, J.-S. Tsai, and T. Yamamoto, *Nat. Commun.* **5**, 4480 (2014).
 - ¹⁹ P. Krantz, A. Bengtsson, M. Simoen, S. Gustavsson, V. Shumeiko, W. D. Oliver, C. M. Wilson, P. Delsing, and J. Bylander, *Nat. Commun.* **7**, 11417 (2016).
 - ²⁰ W. Wustmann and V. Shumeiko, *Phys. Rev. Appl.* **8**, 024018 (2017).
 - ²¹ M. Simoen, C. W. S. Chang, P. Krantz, J. Bylander, W. Wustmann, V. Shumeiko, P. Delsing, and C. M. Wilson, *J. Appl. Phys.* **118**, 154501 (2015).
 - ²² E. Zakka-Bajjani, F. Nguyen, M. Lee, L. R. Vale, R. W. Simmonds, and J. Aumentado, *Nat. Phys.* **7**, 21 (2011).
 - ²³ B. Abdo, K. Sliwa, F. Schackert, N. Bergeal, M. Hatridge, L. Frunzio, A. D. Stone, and M. Devoret, *Phys. Rev. Lett.* **110**, 173902 (2013).
 - ²⁴ A. Heidmann, R. J. Horowicz, S. Reynaud, E. Giacobino, C. Fabre, and G. Camy, *Phys. Rev. Lett.* **59**, 2555 (1987).
 - ²⁵ R. Graham and H. Haken, *Z. Phys.* **210**, 276 (1968).
 - ²⁶ K. J. McNeil and C. W. Gardiner, *Phys. Rev. A* **28**, 1560 (1983).
 - ²⁷ S. Reynaud, *EPL (Europhysics Letters)* **4**, 427 (1987).
 - ²⁸ A. Lane, M. Reid, and D. Walls, *Phys. Rev. A* **38**, 788 (1988).
 - ²⁹ C. Fabre, E. Giacobino, A. Heidmann, and S. Reynaud, *J. Phys. (Paris)* **50**, 1209 (1989).
 - ³⁰ G. Björk and Y. Yamamoto, *Phys. Rev. A* **37**, 1991 (1988).
 - ³¹ M. D. Reid and P. D. Drummond, *Phys. Rev. A* **40**, 4493 (1989).
 - ³² J. Y. Courtois, A. Smith, C. Fabre, and S. Reynaud, *J. Mod. Opt.* **38**, 177 (1991).
 - ³³ L. Spietz, K. W. Lehnert, I. Siddiqi, and R. J. Schoelkopf, *Science* **300**, 1929 (2003).
 - ³⁴ R. H. Koch, J. Clarke, W. M. Goubau, J. M. Martinis, C. M. Pegrum, and D. J. Van Harlingen, *J. Low Temp. Phys.* **51**, 207 (1983).
 - ³⁵ R. Adler, *Proc. IRE* **34**, 351 (1946).
 - ³⁶ J. Jing, S. Feng, R. Bloomer, and O. Pfister, *Phys. Rev. A* **74**, 041804 (2006).
 - ³⁷ A. Pikovsky, M. Rosenblum, and J. Kurths, *Synchronization: a universal concept in nonlinear sciences*, Vol. 12 (Cambridge university press, 2003).